# Thickness-Dependent Structure–Property Relationships in Strained (110) $SrRuO_3$ Thin Films

*Daisuke Kan,* Ryotaro Aso, Hiroki Kurata, and Yuichi Shimakawa*

**Thickness-dependent structure–property relationships in strained $SrRuO_3$ thin films on $GdScO_3$ (GSO) substrates are reported. The film is found to have epitaxially stabilized crystal structures that vary with the film thickness. Below 16 nm, the $\sqrt{2}a_{pc} \times \sqrt{2}a_{pc} \times 2a_{pc}$ monoclinic structure is stabilized while above 16 nm the film has the $a_{pc} \times 2a_{pc} \times a_{pc}$ tetragonal structure. The thickness-dependent structural changes are ascribed to the substrate-induced modification in the $RuO_6$ octahedral rotation pattern, which highlights the significance of the octahedral rotations for the epitaxial strain accommodation in the coherently-grown films. Close relationships between the structural and physical properties of the films are also found. The monoclinic film has the uniaxial magnetic easy axis 45° away from the $[110]_{GSO}$ direction while the tetragonal film has the one that lies along the in-plane $[1\text{–}10]_{GSO}$ direction. The results demonstrate that the octahedral rotations in the strained perovskite oxide thin films are a key factor for determining their structure phases and physical properties.**

## 1. Introduction

Perovskite oxides $ABO_3$ have attracted a great deal of attentions due to their variety of functional properties resulting from strong correlations between lattices, electrons and spins.[1] Recent progresses in atomic-scale synthesis of the oxides have demonstrated that these functional properties are further expanded through the fabrications of oxide-based epitaxial heterostructures[2–5] and superlattices.[6–8] An important consequence of the heteroepitaxial growth is that the films grow in such a way that the film and substrate has the identical in-plane lattice parameters and that the film suffers from the epitaxial strain provided by the lattice mismatch between the film and the substrate. In fact, it has been theoretically and experimentally revealed that such strain accommodation results in distortions in the backbone of the perovskite structure that consists of the corner-sharing $BO_6$ octahedra, including deformations (changes in size) of the octahedra, cation displacements within the octahedra and cooperative rotations (or tilting) of the octahedra, which have consequently profound influence on the physical properties. Besides, recent theoretical studies[9–13] have suggested that even in the strained film of which in-plane lattice parameters are fixed by the substrate, there are still degrees of freedom in octahedral rotations in the perovskite framework. It is thus indispensable to learn how the substrate-induced strain is accommodated into the perovskite lattice of the films and how the strain accommodation affects their structural and physical properties.

To this end, our focus is on itinerant ferromagnet $SrRuO_3$ (SRO) which exhibits structural phase transitions associated with $RuO_6$ octahedral rotations. In bulk, SRO has the *Pbmn* orthorhombic structure with the $\sqrt{2}a_{pc} \times \sqrt{2}a_{pc} \times 2a_{pc}$ unit cell dimension at room temperature,[14] in which the $RuO_6$ octahedral rotation in the pattern described as $a^-a^-c^+$ in the Glazer notation[15] is formed as a result of the mismatch between the Sr-O and $\sqrt{2}$(Ru-O) bond lengths. $a_{pc}$ denotes the pseudocubic perovskite lattice parameter. As the temperature is raised from room temperature, the orthorhombic phase undergoes the phase transition to the *I4/mcm* tetragonal phase with the $\sqrt{2}a_{pc} \times \sqrt{2}a_{pc} \times 2a_{pc}$ unit cell and the $a^0a^0c^-$ rotation pattern at 547 °C, which is followed by another transition to the *Pm3m* cubic phase with the $a_{pc} \times a_{pc} \times a_{pc}$ unit cell at 677 °C. Recently, it has been shown that, when SRO is grown into an epitaxial thin film form, the film structure and its structural transition are strongly affected by the degree of the strain provided by the substrate,[16–19] implying the significant role of the $RuO_6$ octahedral rotation on the epitaxial strain accommodation. However, it has not been fully explored how such substrate-induced strain accommodation in the films with the in-plane lattice spacing fixed by the substrate affects their structural phase and, as a consequence, their physical properties.

This paper reports on the thickness-dependent structure-property relationships in the straiend SRO thin films. We find that for the film thinner than 16 nm, the monoclinic structure with the $\sqrt{2}a_{pc} \times \sqrt{2}a_{pc} \times 2a_{pc}$ unit cell is epitaxially stabilized while the film thicker than 16 nm has the tetragonal structure with the cell-doubled $a_{pc} \times 2a_{pc} \times a_{pc}$ unit cell. The results of detailed structural characterizations indicate that the thickness-dependent structure change is ascribed to the substrate-induced modification in the $RuO_6$ octahedral rotation pattern in the strained film which has in-plane lattice parameters that are fixed by the substrate. We further demonstrate that physical properties are closely correlated with the film structure. The

Dr. D. Kan, R. Aso, Prof. H. Kurata, Prof. Y. Shimakawa
Institute for Chemical Research
Kyoto University and Japan Science and Technology Agency
CREST, Uji, Kyoto 611-0011, Japan
E-mail: dkan@scl.kyoto-u.ac.jp

DOI: 10.1002/adfm.201202402

monoclinic film has the ferromagnetic transition temperature, $T_c$ which increases up to 130 K with increasing the thickness while the tetragonal film has $T_c \approx 100$ K independent of the thickness. The magnetic anisotropy is also strongly affected by the film structures, indicating the importance of the magnetocrystalline effect in SRO. The results highlight that the epitaxial strain accommodation through the octahedral rotations in the strained SRO films plays a significant role in determining their structural phase and physical properties.

## 2. Results and Discussions

We fabricated SRO thin films on the orthorhombic (110) $GdScO_3$ (GSO) substrates. Based on the lattice mismatch between the bulk SRO ($a$ = 5.57 Å, $b$ = 5.53 Å, and $c$ = 7.85 Å) and the substrate ($a$ = 5.45 Å, $b$ = 5.75 Å, $c$ = 7.93 Å), the film suffers from the tensile strain of +0.96% and +1.09% along the $[1\text{–}10]_{GSO}$ and $[001]_{GSO}$ directions, respectively. Hereafter the orthorhombic notation are used for the indices unless otherwise indicated. To obtain the strained films with an atomically smooth surface, the substrate were annealed in air and chemically etched with NaOH solution[20] prior to the film growth by pulsed laser deposition. The films were grown at 700 °C under the oxygen partial pressure of 100 mTorr. For more details, see the Experimental Section.) We confirmed from atomic force microscopy observations that the fabricated films have step-and-terrace surface structure with single pseudo-cubic unit cell height steps (≈4 Å) as shown in the inset of **Figure 1**a. Figure 1a shows X-ray $2\theta$–$\theta$ profiles of the fabricated films with the thicknesses ranging from 10 to 25 nm. We see reflections only from the film and substrate without any peaks from a secondary phase. Besides, the interference fringes (Laue oscillations) of which period correspond to the film thickness are observed. As shown in Figure 1b, the full width at half maximum (FWHM) of (220) SRO reflection is found to be as small as ≈0.07° for all fabricated films. These observations ensure the high-quality of the fabricated films. In Figure 1c, we plot the out-of-plane lattice spacing $d_{110}$ ($d_{010\_pc}$) of the films as a function of the film thickness. It is seen that $d_{110}$ slightly increases below 16 nm, hinting that the film structure depends on the thickness.

To further investigate the film structure, we performed reciprocal space mappings around (620), (444), (260) and (44–4) GSO Bragg reflections. The results for the 15.2-nm and 24.9-nm thick films are presented in **Figure 2**a,b, respectively. For both films, no multiple reflections from the SRO layer are observed in each mapping and all reflections from the film layer are seen in the same position along the in-plane direction (the horizontal axis), confirming that the in-plane lattice spacing is fixed by the substrate and that the single crystallographic domain films coherently grown on the substrates, regardless of the thickness. Importantly, for the 15.2-nm-thick film in Figure 2a, (620) and (260) SRO reflections appear at different positions along out-of-plane direction (the vertical axis) while these reflections for the thicker film (Figure 2b) are seen at the same position. This indicates that the thinner film has a lower symmetry structure than an orthorhombic one with $a \neq b$ whereas the thicker film has a tetragonal structure.

In **Figure 3** we presented the cross-sectional TEM images and nano-beam electron diffraction (NBED) patterns observed for the thinner and thicker films. The TEM images (Figure 3a,d) show that for both films, there are no misfit dislocations at the interface between the film and substrate, which is consistent with the fact of the coherent film growth irrespective of the film structures. In the NBED patterns for the thinner film (Figure 3b,c) we see the $1/2\{110\}_{pc}$ (circled in red in Figure 3b) and $1/2\{001\}_{pc}$ superstructure spots (circled in orange in Figure 3c) in addition to the fundamental spots. (The $[010]_{pc}$ direction is defined as the one parallel to the out-of-plane direction as depicted in **Figure 4**a,b) In contrast, for the thicker film, no $1/2\{110\}_{pc}$ spots are seen and instead the $1/2\{010\}_{pc}$ spots (circled in blue in Figure 3e,f) are visible which indicates that the cell-doubling takes place along the $[010]_{pc}$ direction (along the out-of-plane direction).

On the basis of our experimental results, we derived the unit cells of the thin and thick SRO films, which are schematically shown in Figure 4a,b, respectively. For the thin film where $a > b$, the unit cell dimension is $\sqrt{2}a_{pc} \times \sqrt{2}a_{pc} \times 2a_{pc}$ (drawn in the red solid line), which is similar to the bulk orthorhombic unit cell. As the films are coherently grown under the tensile strain in such way that the (110) plane of the film is parallel to the one

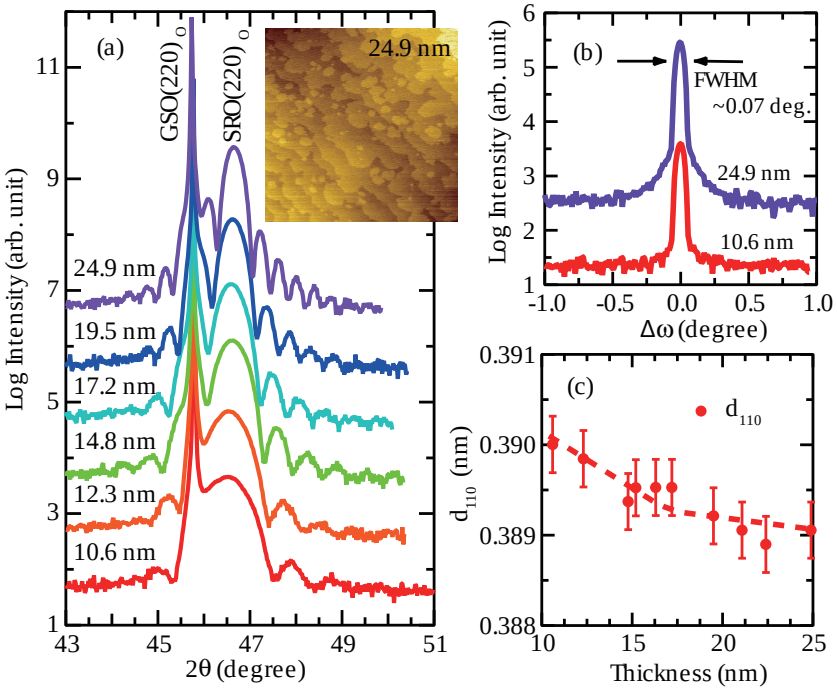


**Figure 1.** a) X-ray $2\theta$–$\theta$ diffraction patterns for (110) $SrRuO_3$ (SRO) epitaxial thin film with various thicknesses. The inset shows the AFM surface morphology of the 24.9-nm-thick films. b) Omega scan of the (220) SRO Bragg reflections of 10.6- and 24.9-nm-thick films. c) Out-of-plane lattice spacing $d_{110}$ of the films as a function of the film thickness.

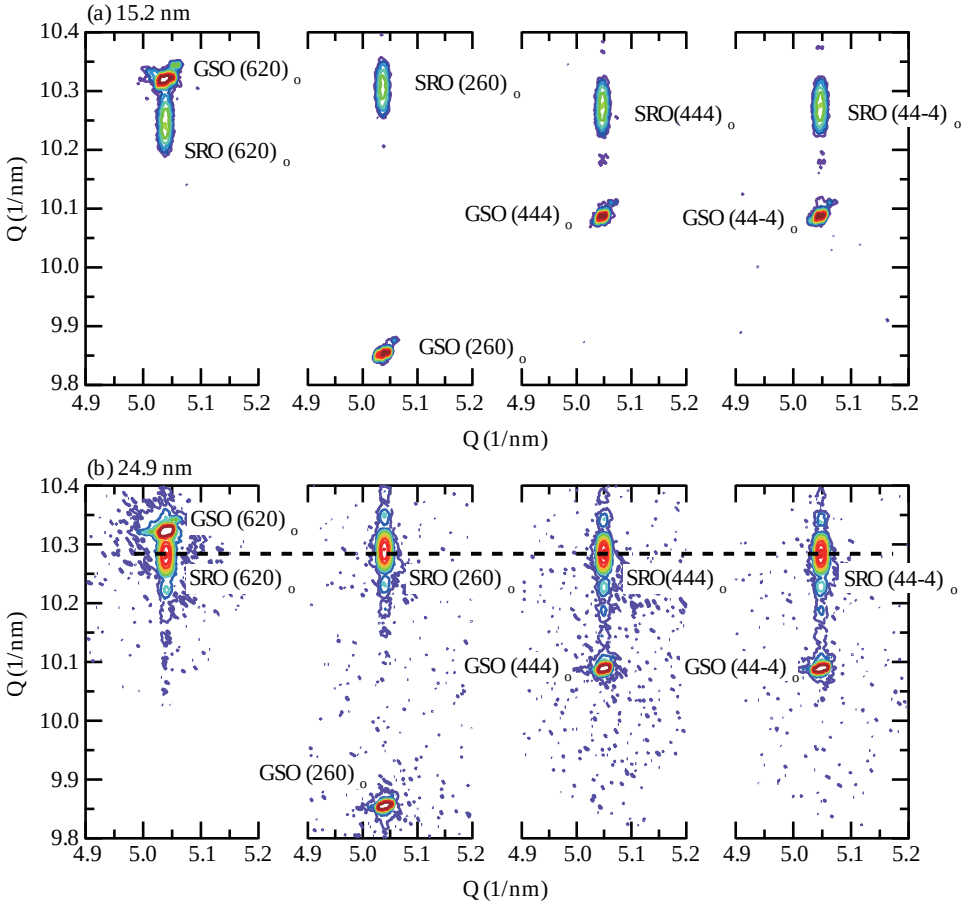


**Figure 2.** Semilogarithmic contour plots of reciprocal space mappings around (620), (444), (260), and (44–4) $GdScO_3$ (GSO) Bragg reflections for the a) 15.2-nm and b) 24.9-nm-thick films. In each mapping, the vertical and horizontal axes correspond to the out-of-plane and in-plane direction of the film, respectively. All mappings were recorded at room temperature. The reflections are indexed with the orthorhombic notation.

of the substrate (Figure 1b), the angle $\gamma$ is ≈91°, larger than 90° and, as a result, the pseudo-cubic perovskite unit cell (drawn in the black dotted line) is distorted with $\alpha_{pc}$ (≠ 90°) as depicted in Figure 4a. This is consistent with the fact that the structural symmetry for the thinner film is monoclinic which can be regarded as the distorted orthorhombic structure. Since the orthorhombic structrure in bulk SRO results from the cooperative $RuO_6$ octahedral rotations, it is reasonable to consider that the monoclinic (distorted orthorhombic) films have the octahedral rotations that resemble the bulk sample with the $a^-a^-c^+$ rotation pattern. For the thick films where $a = b$, the unit cell dimension is found to be $a_{pc} \times 2a_{pc} \times a_{pc}$ (drawn in the black solid line in Figure 4b) with no distortion in $\alpha_{pc}$ indicating that the thick films have a tetragonal structure. Since the in-plane lattice spacing along the $[001]_{GSO}$ and $[1\text{–}10]_{GSO}$ directions of the monoclinic and tetragonal films, respectively, remains unchanged, the results indicate that the $RuO_6$ octahedral rotation pattern is different between these films.

For the tetragonal phase, the fact that the unit cell is $a_{pc} \times 2a_{pc} \times a_{pc}$ indicates that there are neither octahedral rotations nor tilts. When an octahedron in the perovskite structure is rotated or tilted in a given way, it requires rotations or tilts of the neighboring octahedra, and thus the unit cell becomes larger than the fundamental perovskite one. We also note that the corner sharing connectivity of the octahedra in the perovskite lattice requires changes in the unit cell dimension along at least two axes. For example, the rotation of the octahedral about the $[001]_{pc}$ axis changes the fundamental perovskite lattice from $a_{pc} \times a_{pc} \times a_{pc}$ to $\sqrt{2}a_{pc} \times \sqrt{2}a_{pc} \times a_{pc}$ (#21 Glazer tilt system) or $\sqrt{2}a_{pc} \times \sqrt{2}a_{pc} \times 2a_{pc}$ (#22).[15,21] Therefore, the $a_{pc} \times 2a_{pc} \times a_{pc}$ tetragonal film thicker than 16 nm has no octahedral rotation. A possible origin of the cell-doubling along the $[010]_{pc}$ (out-of-plane) direction is anti-parallel cation or oxygen displacements. Because no apparent cation displacements are observed in the TEM image (Figure 3d), the cell-doubling arises more likely from the oxygen displacements.

To further evaluate the phase stability of the monoclinic and tetragonal structures, we measured temperature dependence of out-of-plane lattice spacing $d_{110}$ of the films. The results in Figure 4c show that $d_{110}$ (out-of-plane lattice spacing) linearly increases with the temperature and that there is no signature of temperature-induced structural transition, which is in close agreement with the previous report.[17] This implies that each monoclinic and tetragonal phase is epitaxially stabilized by the

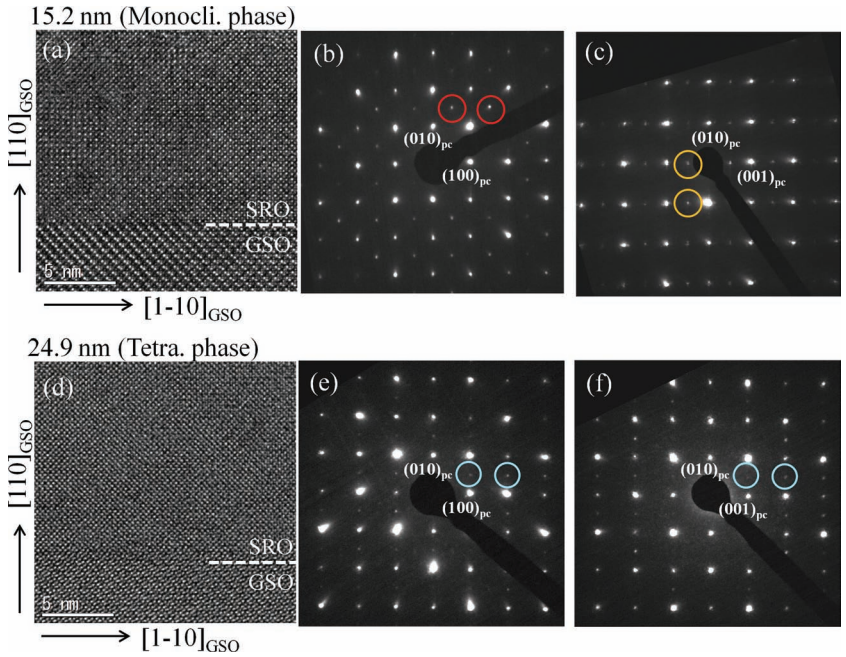


**Figure 3.** a,d) Cross-sectional TEM images and b,c,e,f) nanobeam electron diffraction patterns for the monoclinic and tetragonal films. For (b) and (e), the diffraction patterns are recorded in [001] zone. The incident electron beam is parallel to the [001] direction (the $[001]_{pc}$ direction). For (c) and (f) the diffraction patterns are recorded in [1–10] zone. The electron beam is parallel to the [1–10] direction (the $[100]_{pc}$ direction). For electron diffraction patterns, the diffraction spots are indexed with the pseudo-cubic notation.

substrate and is formed at the deposition temperature, 700 °C, where SRO inherently has the cubic structure. Given that at the deposition temperature the GSO substrate still maintains the $a^-a^-c^+$ octahedral rotation pattern[22] which is the same as the one of the bulk orthorhombic SRO, the octahedral rotations in the monoclinic (distorted orthorhombic) film emerges as a result of the matching in the rotation pattern between the film and substrate. For the tetragonal films where no octahedral rotations are included, it can be regarded as the inherent cubic structure with the deformed octahedra due to the substrate-induced tensile strain.

Figure 4d presents the thickness dependence of the lattice constants at room temperature, which were obtained from the $d_{620}$, $d_{260}$ and $d_{110}$ values of the films. We note that for all films the lattice constant $c$ (parallel to the $[001]_{GSO}$ direction) is identical to the $d_{001}$ value of the substrate 7.93 Å. It is seen that the structural change from the monoclinic phase with $a$ = 5.57 Å and $b$ = 5.54 Å to the tetragonal phase with $a = b$ = 5.56 Å occurs around 16 nm. This behavior indicates that the tetragonal structure is the most stable one when the in-plane lattice spacing of the GSO substrate are imposed on SRO and that the elastic strain energy due to the octahedral rotation induced by the substrate crystal structure is accommodated up to the film thickness of 16 nm.

We also found close relationships between the structural and physical properties of the films. **Figure 5**a shows the temperature dependence of resistivity $\rho_{xx}$ of the films with the monoclinic and tetragonal structures. While each film exhibits metallic conductions down to 10 K with a kink in the $\rho_{xx}$–$T$ curve due to the ferromagnetic transition, the $\rho_{xx}$ value is larger and the transition temperature $T_c$ is lower as compred to those of the films under the compressive strain, for example, the ones on $SrTiO_3$ substrates[23,24] where the $\rho_{xx}$ value at room temperature is 200–300 μΩcm and $T_c$ is ≈150 K. It is also seen that the residual resistance ratio (RRR) defined by $\rho_{xx}(300\ K)/\rho_{xx}(10\ K)$ for the films on GSO substrates is ≈3 and that this value is lower than that for the compressively-strained ones on STO of which RRR is typically 5–10.[23] These indicate that the metallic conduction is suppressed under the tensile strain which reduces covalency in Ru-O bonds along the in-plane directions of the films. In Figure 5b, $T_c$ is plotted against the film thickness revealing the structure dependence of $T_c$. For the monoclinic phase below 16 nm, $T_c$ decreases from 130 K for 15.2-nm-thick film to 103 K for 10.6-nm-thick one. The reduced $T_c$ is probably attributed to the finite size effect,[24] which implies that the monoclinic structure films intrinsically have $T_c$ comparable to be ≈130 K. For the tetragonal structure film above 16 nm, $T_c$ is 100 K independent of the film thickness (in the thickness range studided here).

To further elucidate effects of the thickness-dependent film structures on their properties, we measured the transverse Hall resisitivity $\rho_{xy}$, which consists of the ordinary and anomalous parts. For the ordinary part $R_oH$, where $R_o$ and $H$ are an ordinary Hall coefficient and a magnetic field, respectively, the coefficient $R_o$ is inversely proportional to the charge density $n$. The anomalous part $\rho_{AHE}$ is associated with the magnetization $M$, and is therefore a good measure of magnetic orderings and/or magnetic anisotropy for thin film samples. **Figure 6**a displays the field dependence of $\rho_{xy}$ at 10 K for the 15.2-nm (monoclinic structure) and 24.9-nm-thick (tetragonal structure) films. The data were taken with a current and a magnetic field applied along $[001]_{GSO}$ and $[110]_{GSO}$ directions, respectively. For both films, the ordinary parts in $\rho_{xy}$ are found to be negative. From the slopes ranging from 2 to 6 Tesla, the carrier densities for the 15.2-nm and 24.9-nm-thick films are estimated to be $3.1 \times 10^{22}$ cm$^{-3}$ and $2.2 \times 10^{22}$ cm$^{-3}$, respectively. These values are in close agreement with previous reports[25] where the carrier density of the films under compressive films are reported to be $\approx 3 \times 10^{22}$ cm$^{-3}$. We note that all films investigated in this study have the carrier density of 2–3 $\times 10^{22}$ cm$^{-3}$ independent of the film structure.

In contrast to the ordinary part in $\rho_{xy}$, the anomalous part $\rho_{AHE}$ is strongly dependent on the film structure, reflecting changes in the magnetic anisotropy. As shown in Figure 6a for the monoclinic structure, the square-shaped hysteresis with the corcieve field of 0.5 T is seen, confirming the ferromagnetic ordering and the magnetic moment having a component along the $[110]_{GSO}$ (out-of-plane) direction. On the other hand, $\rho_{AHE}$ for the tetragonal structure exhibits no hysteresis, indicating that the magnetic moment aligns along the in-plane direction of the film. To determine the direction of the magnetic easy

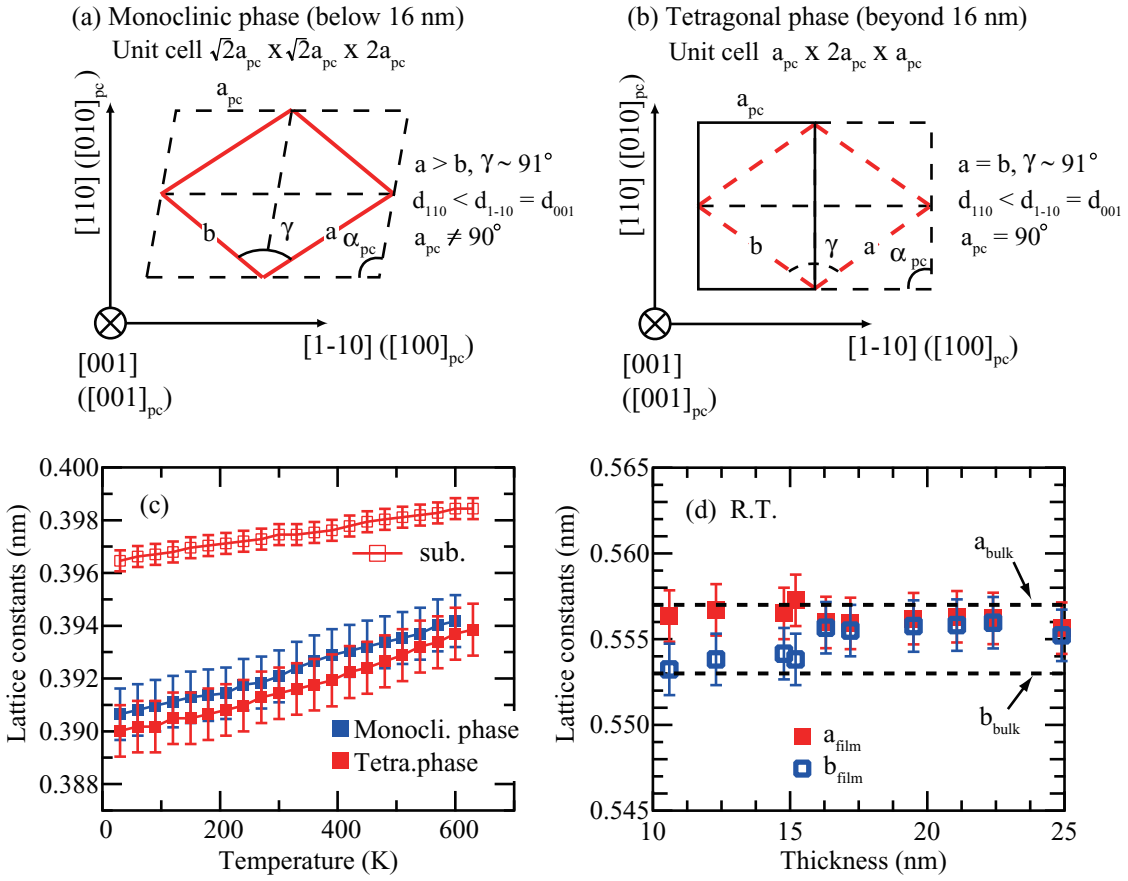


**Figure 4.** a,b) Schematic drawings of the unit cells of the monoclinic and tetragonal films. In the figures, the unit cells of the films are drawn in the thick lines. The subscript pc denotes the pseudo-cubic notation. c) Temperature dependence of the out-of-plane lattice spacing $d_{110}$ ($d_{010\_pc}$) of the films with the monoclinic and tetragonal structures. d) Thickness dependence of lattice constants *a* and *b* (in the orthorhombic notation) of the SRO films.

axis for the monoclinic structre, we also measured the field angle dependence of $\rho_{xy}$ and $\rho_{xx}$. For materials with the strong magnetic anisotropy, such as SRO,[26] the magnetic moment does not follow changes in the direction of the applied field. When the angle between the easy axis and the field exceeds 90°, the reversal of the magnetic moment immediately takes place which is observed as jumps in $\rho_{xy}$ and peaks in $\rho_{xx}$. Figure 6b,c present the field angle ($\theta_H$) dependence of $\rho_{xy}$ of

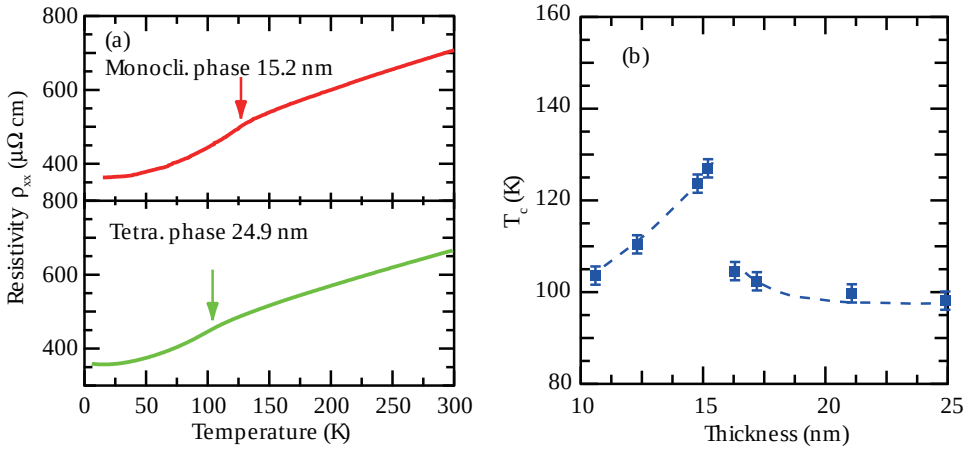


**Figure 5.** a) Temperature dependence of resistivity $\rho_{xx}$ for films with the monoclinic (upper panel) and tetragonal phases (lower panel). b) Thickness dependence of ferromagnetic transition temperature $T_c$. The $T_c$ values (indicated by the arrows in (a)) were determined by the peak position in the temperature derivative of the $\rho_{xx}$ vs temperature curves.

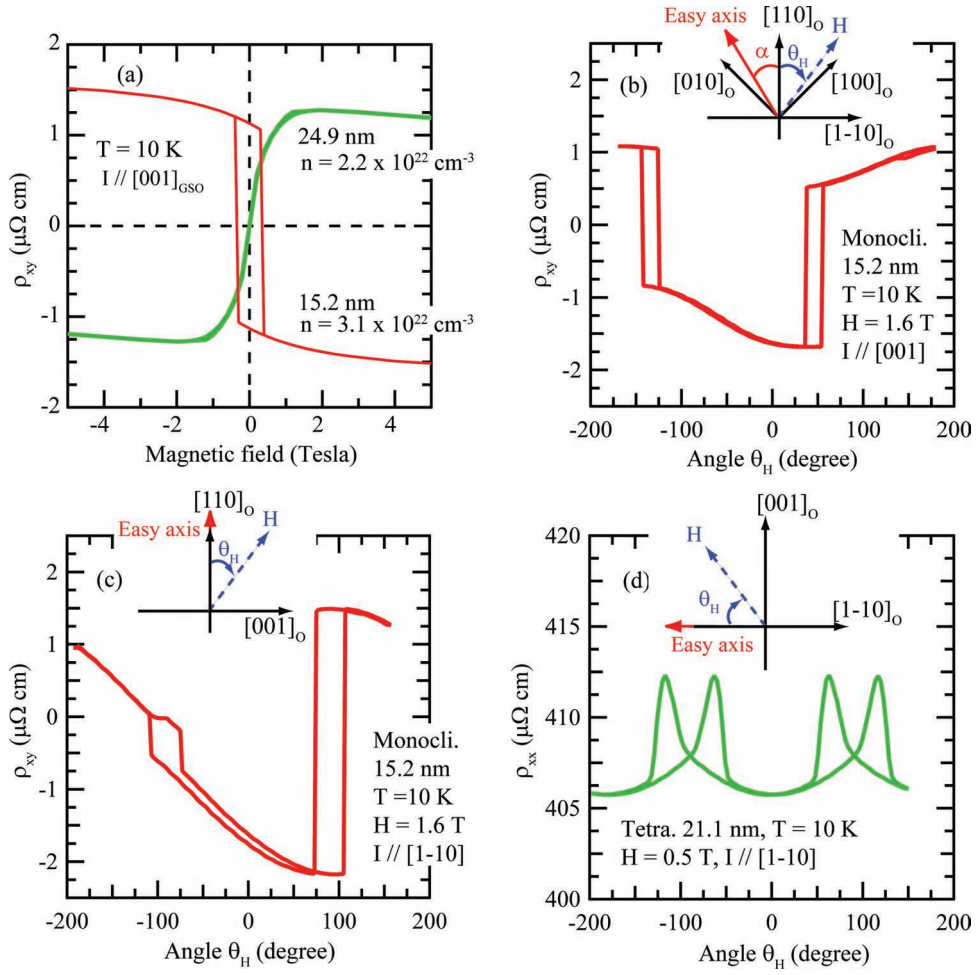


**Figure 6.** a) Magnetic field dependence of hall resistivity $\rho_{xy}$ of the 15.2-nm-monoclinic and 24.9-nm-thick tetragonal films at 10 K. For the measurements, the current and magnetic field were applied along the $[001]_{GSO}$ and $[110]_{GSO}$ directions, respectively. b,c) Field angle $\theta_H$ dependence of the Hall resistivity $\rho_{xy}$ of the 15.2-nm-thick orthorhombic films. In (b), the currents were applied to the [001] direction and the magnetic fields of 1.6T were rotated in the (001) plane. In (c) the excitation current flows along the [1–10] direction and the magnetic field of 1.6 T was applied in the $(1–10)_{GSO}$ plane. d) Field angle $\theta_H$ dependence of the resistivity $\rho_{xx}$ of the 21.1-nm-thick tetragonal film. The data were acquired with the configuration where the excitation current flows the $[1–10]_{GSO}$ direction and the applied magnetic field of 0.5 T is rotated in the $(110)_{GSO}$ plane. In (b–d), the definition of the field angle is given in each inset.

the 15.2-nm-thick monoclinic films under 1.6 T magnetic field applied in the (001) and (1–10) plane, respectively. The definition of the field angle $\theta_H$ is shown in the inset of each figure. $\rho_{xy}$ shows the clear jumps with the hysteresis in the clockwise and counter-clockwise field rotations due to the field-induced magnetization reversal. The jump in $\rho_{xy}$ is observed at every 180° in $\theta_H$, revealing the uniaxial magnetic anisotropy of the monoclinic films. From the center angle of the hysteresis, the easy axis angle $\alpha$ for the 15.2-nm-thick film is determiend to be 41.5° tilted from the [110] direction toward the [100] direction. The definition of $\alpha$ is also given in the inset of Figure 6b. We note that the magnetic moment of the monoclinic film is confined in (001) plane, which is verified by the fact that when the magnetic field is applied in the (110) plane (Figure 6c), the hysteresises in $\rho_{xy}$ are seen at ±90° in the field angle $\theta_H$.

For the tetragonal phase where the magnetic moment lies in the (110) plane, we measured $\rho_{xx}$ under the in-plane magnetic field to identify the easy axis direction. Figure 6d displays the field angle dependence of $\rho_{xx}$ under a 0.5 T magnetic field in the (110) plane for the 21.1-nm-thick tetragonal film. We see peaks in $\rho_{xx}$ due to the field-induced magnetization reversal in the clockwise and counter-clockwise field rotations. The peaks are observed at every 180° in $\theta_H$ and that the center of the peaks in the clockwise and counter-clockwise field rotations lies at ±90° in $\theta_H$. This indicates that the tetragonal film has the uniaxial magnetic anisotropy with the easy axis parallel to the $[1–10]_{GSO}$ direction. **Figure 7** presents the thickness dependence of the easy axis angle $\alpha$. The monoclinic structure film has the easy axis ≈45° tilted from the [110] direction while for the tetragonal film the easy axis is along the $[1–10]_{GSO}$ direction. In each monoclinic and tetragonal structure, no obvious thickness

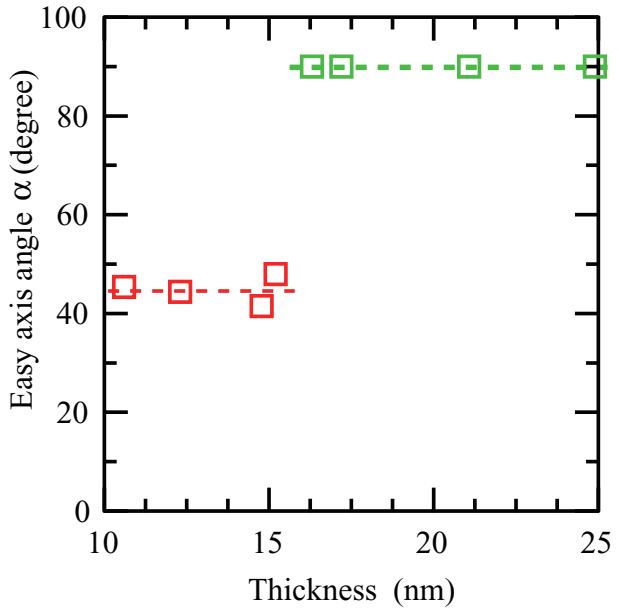


**Figure 7.** Magnetic easy axis angle $\alpha$ plotted against the film thickness. The definition of the easy axis angle $\alpha$ is given in the inset of Figure 6b.

dependence is observed. Instead, the easy axis direction changes in response to the thin film structure change taking place at the film thickness of 16 nm. This indicates that the magnetocrystalline effect plays an important role on the magnetic anisotropy in SRO.

## 3. Conclusions

We investigated the structure-property relationships in the coherently-grown (110) SRO thin films on the $GdScO_3$ substrates. We found that the thin film has the thickness dependent epitaxially-stabilized structure. The films thinner than 16 nm has the $\sqrt{2}a_{pc} \times \sqrt{2}a_{pc} \times 2a_{pc}$ monoclinic structure while those with a larger thickness has the $a_{pc} \times 2a_{pc} \times a_{pc}$ tetragonal structure. The thickness dependent film structures result from the substrate-induced changes in the $RuO_6$ octahedral rotation pattern. This highlights the significance of the octahedral rotations for the epitaxial strain accommodation in the coherently grown films. We also revealed the close relationships between the film structure and physical properties. The monoclinic film has the ferromagnetic transition temperature $T_c$ which increases up to 130 K as the thinckness increases while the tetragonal film has $T_c \approx 100$ K independent of the thickness. The magnetic easy axis for the monoclinic film lies at ≈45° away toward the [100] direction from the [110] direction while the teragonal film has the easy axis parallel to the $[1\text{–}10]_{GSO}$ direction, indicating the importantance of the magnetocrystalline effect on the magnetic anisotropy in SRO. Our results demonstrate the critical role of the octahedral rotations in the strain accommodation in the coherently grown films, which are the key factor for determining their structure and physical properties.

## 4. Experimental Section

$SrRuO_3$ epitaxial thin films with thicknesses ranging from 10 to 25 nm were fabricated on $(110)_{ortho}$ $GdScO_3$ (GSO) substrates by pulsed laser deposition. The subscript ortho denotes the orthorhombic notation. The lattice parameters of the substrates are $a_{ortho}$ = 5.45 Å, $b_{ortho}$ = 5.75 Å, $c_{ortho}$ = 7.93 Å for GSO. The corresponding lattice mismatch between SRO ($a_{ortho}$ = 5.57 Å, $b_{ortho}$ = 5.53 Å, and $c_{ortho}$ = 7.85 Å in bulk) and the substrate, $(a_{sub}\text{-}a_{SRO})/a_{SRO}$ where $a_{sub}$, $a_{SRO}$ are the pseudo-cubic lattice parameter of the substrate and SRO, respectively is +0.96% along the $[1\text{–}10]_{GSO}$ direction and +1.09% along the $[001]_{GSO}$ direction. Before the film deposition, the substrates were annealed in air and etched by NaOH aqueous solution to prepare the atomically smooth surfaces with single unit cell height steps (≈4 Å). We used the Ru-rich $SrRu_{1.1}O_3$ target to minimize possible Ru deficiency in the films, which would deteriorate film's quality. During the deposition, the target was ablated using the KrF excimer laser ($\lambda$ = 248 nm, Coherent COMPex-Pro 205 F) with a laser spot density of 1.0 J/cm$^2$ at the target with a spot area of 5 × 2 mm$^2$, and the substrate temperature and partial oxygen pressure were kept at 700 °C and 100 mTorr, respectively.

Structural characterizations of the fabricated thin films were carried out using a conventional four-circle diffractometer (PANalytical X'Pert MRD) equipped with the hot sample stage (DHS1100). Surface morphology of the fabricated films was observed by atomic force microscope with a tapping mode at room temperature. For cross-sectional TEM observations, the specimens were thinned down to electron transparency by mechanical polishing and Ar-ion milling. The TEM observations were performed at room temperature using JEM-2200FS equipped with a spherical aberration corrector (CEOS CETOCOR) for imaging lens system. Since the thickness of fabricated SRO films was thinner than 25 nm, the electron diffraction patterns were recorded in a nano beam mode where the electron beam was focused down to 10 nm in diameter allowing the collection of the pattern from only the film region. The nanobeam electron diffraction (NBED) was done by using the smallest condenser aperture with a 10-μm diameter and focusing the electron beam at the front of the focal plane of the objective pre-field. TEM images and NBED patterns were recorded on a 2000 × 2000 CCD camera (Ultrascan, Gatan, USA).

For transport measurements, the fabricated films are patterned into 50-μm-wide hall bars by conventional photolithography and Ar-ion milling. The longitudinal and transverse Hall resistivity ($\rho_{xx}$ and $\rho_{xy}$) were measured in a conventional 4-terminal configuration. The magnetic field angle dependence of $\rho_{xx}$ and $\rho_{xy}$ was evaluated using physical property measurement system (PPMS, Quantum Design) equipped with a sample rotator.

## Acknowledgements

This work was partially supported by Grants-in-Aid for Scientific Research (Grants No. 19GS0207 and No. 24760009) and a grant for the Project of Integrated Research on Chemical Synthesis from the Ministry of Education, Culture, Sports, Science and Technology of Japan. The work was also supported by Japan Science and Technology Agency's CREST program.

Received: August 22, 2012
Published online: October 4, 2012

[1] M. Imada, A. Fujimori, Y. Tokura, *Rev. Mod. Phys.* **1998**, *70*, 1039.
[2] K. J. Choi, M. Biegalski, Y. L. Li, A. Sharan, J. Schubert, R. Uecker, P. Reiche, Y. B. Chen, X. Q. Pan, V. Gopalan, L.-Q. Chen, D. G. Schlom, C. B. Eom, *Science* **2004**, *306*, 1005.
[3] A. Ohtomo, H. Y. Hwang, *Nature* **2004**, *427*, 423.
[4] J. H. Lee, L. Fang, E. Vlahos, X. Ke, Y. W. Jung, L. F. Kourkoutis, J.-W. Kim, P. J. Ryan, T. Heeg, M. Roeckerath, V. Goian, M. Bernhagen, R. Uecker, P. C. Hammel, K. M. Rabe, S. Kamba,

J. Schubert, J. W. Freeland, D. A. Muller, C. J. Fennie, P. Schiffer, V. Gopalan, E. Johnston-Halperin, D. G. Schlom, *Nature* **2010**, *466*, 954.
[5] R. J. Zeches, M. D. Rossell, J. X. Zhang, A. J. Hatt, Q. He, C.-H. Yang, A. Kumar, C. H. Wang, A. Melville, C. Adamo, G. Sheng, Y.-H. Chu, J. F. Ihlefeld, R. Erni, C. Ederer, V. Gopalan, L. Q. Chen, D. G. Schlom, N. A. Spaldin, L. W. Martin, R. Ramesh, *Science* **2009**, *326*, 977.
[6] H. N. Lee, H. M. Christen, M. F. Chisholm, C. M. Rouleau, D. H. Lowndes, *Nature* **2005**, *433*, 395.
[7] E. Bousquet, M. Dawber, N. Stucki, C. Lichtensteiger, P. Hermet, S. Gariglio, J.-M. Triscone, P. Ghosez, *Nature* **2008**, *452*, 732.
[8] A. V. Boris, Y. Matiks, E. Benckiser, A. Frano, P. Popovich, V. Hinkov, P. Wochner, M. Castro-Colin, E. Detemple, V. K. Malik, C. Bernhard, T. Prokscha, A. Suter, Z. Salman, E. Morenzoni, G. Cristiani, H.-U. Habermeier, B. Keimer, *Science* **2011**, *332*, 937.
[9] A. T. Zayak, X. Huang, J. B. Neaton, K. M. Rabe, *Phys. Rev. B* **2006**, *74*, 094104.
[10] J. M. Rondinelli, N. A. Spaldin, *Phys. Rev. B* **2010**, *82*, 113402.
[11] J. M Rondinelli, N. A Spaldin, *Adv. Mater.* **2011**, *23*, 3363.
[12] J. M. Rondinelli, S. Coh, *Phys. Rev. Lett.* **2011**, *106*, 235502.
[13] J. He, A. Borisevich, S. V. Kalinin, S. J. Pennycook, S. T. Pantelides, *Phys. Rev. Lett.* **2010**, *105*, 227203.
[14] B. J. Kennedy, B. A. Hunter, *Phys. Rev. B* **1998**, *58*, 653.
[15] A. M. Glazer, *Acta Crystallogr. Sect. B* **1972**, *28*, 3384.
[16] G. Koster, L. Klein, W. Siemons, G. Rijnders, J. S. Dodge, C.-B. Eom, D. H. A. Blank, M. R. Beasley, *Rev. Mod. Phys.* **2012**, *84*, 253.
[17] K. J. Choi, S. H. Baek, H. W. Jang, L. J. Belenky, M. Lyubchenko, C.-B. Eom, *Adv. Mater.* **2010**, *22*, 759.
[18] D. Kan, Y. Shimakawa, *Cryst. Growth Des.* **2011**, *11*, 5483.
[19] S. H. Chang, Y. J. Chang, S. Y. Jang, D. W. Jeong, C. U. Jung, Y.-J. Kim, J.-S. Chung, T. W. Noh, *Phys. Rev. B* **2011**, *84*, 104101.
[20] J. E. Kleibeuker, G. Koster, W. Siemons, D. Dubbink, B. Kuiper, J. L. Blok, C.-H. Yang, J. Ravichandran, R. Ramesh, J. E. Elshof, D. H. A. Blank, G. Rijnders, *Adv. Funct. Mater.* **2010**, *20*, 3490.
[21] P. M. Woodward, *Acta Crystallogr. Sect. B* **1997**, *53*, 32.
[22] M. D. Biegalski, J. H. Haeni, S. Trolier-McKinstry, D. G. Schlom, C. D. Brandle, A. J. Ven Graitis, *J. Mater. Res.* **2005**, *20*, 952.
[23] W. Siemons, G. Koster, A. Vailionis, H. Yamamoto, D. H. A. Blank, M. R. Beasley, *Phys. Rev. B* **2007**, *76*, 075126.
[24] M. Schultz, S. Levy, J. W. Reiner, L. Klein, *Phys. Rev. B* **2009**, *79*, 125444.
[25] P. Khalifah, I. Ohkubo, B. C. Sales, H. M. Christen, D. Mandrus, J. Cerne, *Phys. Rev. B* **2007**, *76*, 054404.
[26] Y. Kats, I. Genish, L. Klein, J. W. Reiner, M. R. Beasley, *Phys. Rev. B* **2005**, *71*, 100403.